Letter

Observation of Majorana-like bound states in metamaterial-based Kitaev chain analogs

Kai Qian,[1,*] David J. Apigo,[1,†] Karmela Padavić,[2,‡] Keun Hyuk Ahn,[1,§] Smitha Vishveshwara,[2,‖] and Camelia Prodan[1,¶]

[1]*Department of Physics, New Jersey Institute of Technology, Newark, New Jersey 07102, USA*
[2]*Department of Physics, University of Illinois at Urbana-Champaign, Urbana, Illinois 61801, USA*

(Received 28 January 2022; accepted 11 October 2022; published 30 January 2023)

We experimentally demonstrate that Majorana-like bound states (MLBSs) can occur in quasi-one-dimensional metamaterials, analogous to Majorana zero modes (MZMs) in the Kitaev chain in terms of mode spectrum and mode wave functions. In a mechanical spinner ladder system, we observe a topological phase transition and spectral-gap-protected edge MLBSs. We characterize phase controllable hybridization and the decaying and oscillatory nature of these MLBS pairs. It is shown that the hybridization can be tuned to yield the analog of parity switching in MZMs. We find strong agreements with theory.

DOI: 10.1103/PhysRevResearch.5.L012012

In the past decade, the rich cross fertilization of ideas between the studies of electronic and mechanical systems has led to the discovery of exciting new states of matter, including physical behaviors driven by topology [1–6]. For example, a Chern insulator with one-way edge modes was demonstrated using an array of gyroscopes [7,8]. Among electronic materials, topological superconductors have gained prominence as candidates for hosting Majorana zero modes (MZMs), which are potential building blocks of fault-tolerant quantum computing [9–20]. The Kitaev chain [21], consisting of electrons hopping on a lattice subject to p-wave pairing, provides an excellent prototype for realizing MZMs as topologically protected edge states [22–25]. Remarkably, these modes have remained elusive in solid state systems despite tremendous efforts [26–33]. Nevertheless, MZMs have continued to inspire experimental realizations of analogous modes in other systems [34,35], including metamaterials. Even key traits for error-free MZM qubits, such as non-Abelian braiding, have recently been proposed in classical metamaterial systems [36].

In this Letter, we present a mechanical metamaterial ladder system made of magnetically coupled spinners, and demonstrate that it closely parallels several salient features of the Kitaev chain, including the distinct presence of Majorana-like bound states (MLBSs). Previous work by two of the current authors and collaborators [37] established a mapping of Hamiltonian matrices between the Kitaev chain and a system of two coupled Su-Schrieffer-Heeger (SSH) chains [38], characterized by alternating bond strengths schematically shown in Fig. 1(b). This further enables the mapping of the mode spectrum, mode wave functions, and the properties that depend only on the mode spectrum and wave functions. A significant benefit of these mappings is that the SSH ladder system can be realized in a variety of bosonic, fermionic, and classical systems. Although MLBSs in these systems may not be exactly equivalent to MZMs, for example, in the ground state degeneracy, which depends on what the SSH ladder is made of, MLBSs are topologically protected by spectral gaps. In a coupled split-ring-resonator system, Guo *et al.* [39] observed one such metamaterial realization of MLBSs and a topological phase transition up to finite size effects. Here, our work on the spinner system explores a topological phase transition for sufficiently long ladders, thus eliminating size effects, and reveals the crucial properties of the MLBS at the edges that were theoretically predicted [37,40–42] but never realized.

In what follows, we demonstrate the remarkable analogs to Kitaev chain features in metamaterials, including spectral characteristics of topological and nontopological phases, oscillatory, decaying MZM wave functions, and switching behavior in fermion parity, which forms the basis of MZM qubits. The Kitaev chain is described by the Hamiltonian [21,37]

$$H_{\mathrm{K}} = \frac{1}{2i}\sum_{n}(\omega-\Delta)a_n b_{n+1} + (\omega+\Delta)a_{n+1}b_n + \mu a_n b_n, \tag{1}$$

where a_n and b_n are the Majorana operators, ω the nearest-neighbor electron hopping amplitude, Δ the p-wave superconducting order parameter, and μ the chemical potential. One of the two topological gapped phases, hosting midgap MZMs, occurs at $|\mu| < 2|\omega|$ and $\Delta > 0$ and the other at

*Present address: Department of Mechanical Aerospace and Engineering, University of California San Diego, La Jolla, California 92093, USA; k3qian@eng.ucsd.edu
†dapigo@gmail.com
‡Present address: Department of Science, Bard High School Early College, New York, New York 10002, USA; kpadavi2@illinois.edu
§kenahn@njit.edu
‖smivish@illinois.edu
¶cprodan@njit.edu

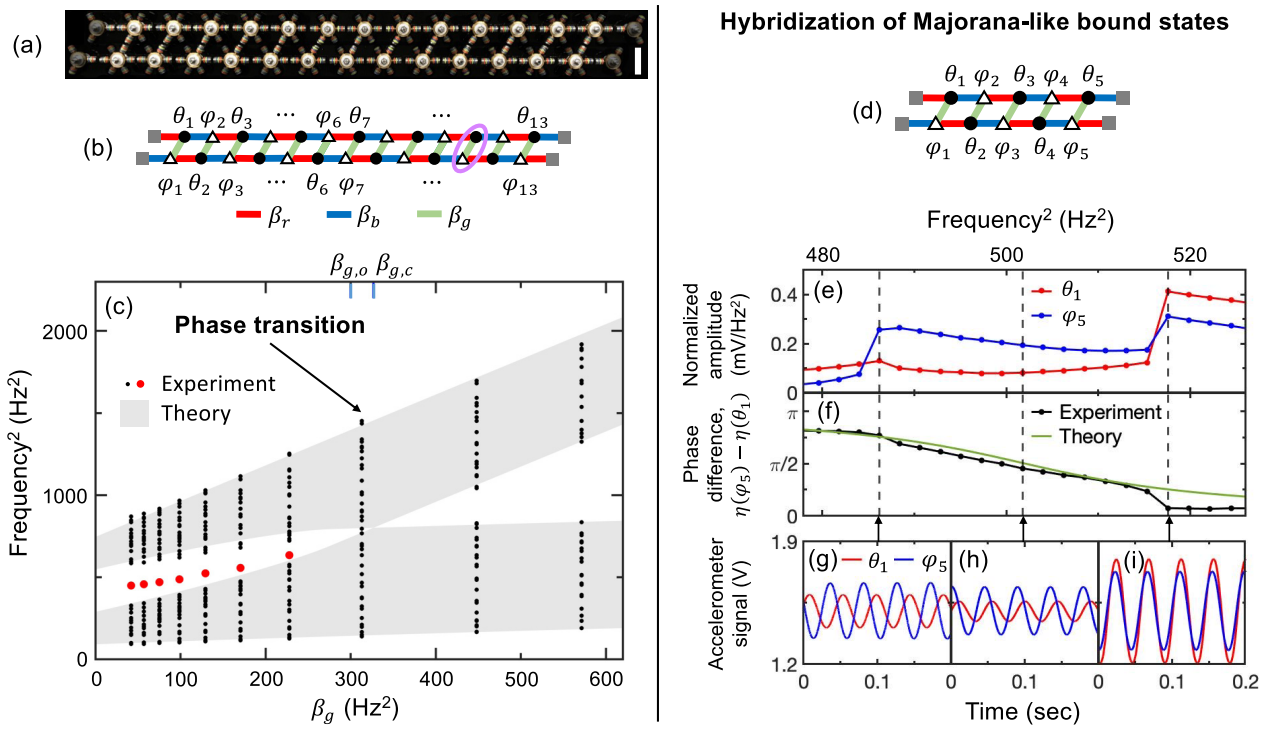

FIG. 1. Phase transition for a long ladder system (left) and phase-controllable hybridized MLBSs for a short ladder system (right). (a) Picture of the experimental setup for a system of length $N = 13$. Rotatable spinners and magnetically coupled arms are highlighted and fixed spinners and arms without magnets are shaded. The scale on the right is 5.0 cm. (b) Schematic diagram for the SSH ladder system pictured in (a). The rotatable spinners are represented by black circles (θ_n) and open triangles (φ_n), and the fixed spinners by gray squares. The purple ellipse shows the unit cell. The red and blue lines denote the *intrachain* coupling $\beta_r = 230$ Hz^2 and $\beta_b = 100$ Hz^2, respectively, and the green line the *interchain* coupling β_g. (c) Topological phase transition for the long $N = 13$ system signaled by the emergence of midgap MLBSs. The measured frequency squared (f^2) for normal mode versus β_g is shown for various interchain coupling β_g. The red dots correspond to the midgap MLBSs, while the black dots correspond to bulk states. The gray areas represent the theoretical bulk bands in the limit of the infinitely long system. The two critical interchain couplings, $\beta_{g,c} = 330$ Hz^2 for the phase transition and $\beta_{g,o} = 300$ Hz^2 for oscillatory MLBSs, are marked on the top axis. (d) Schematic diagram for the short $N = 5$ system. (e) Spectra obtained by actuating the θ_1 spinner and measuring at the θ_1 and φ_5 spinners, shown in red and blue dots, respectively, within the bulk gap for the topological phase with $\beta_g = 100$ Hz^2 and β_r and β_b identical to those for (c). A single degenerate MLBS peak in (c) is split into two MLBS peaks due to the enhanced hybridization. (f) Phase difference between the φ_5 and θ_1 spinners, $\eta(\varphi_5) - \eta(\theta_1)$, versus f^2, revealing phase-controllable MLBSs. (g)–(i): Three examples of the accelerometer signals, proportional to the rotation angles, versus time for lower MLBS, in-between, and upper MLBS, as marked by arrows. The red and blue lines represent the oscillations of the θ_1 and φ_5 spinners. (See Appendix B for typical spectra and gap versus β_g, and see Supplemental Material [47] for videos of modes).

$|\mu| < 2|\omega|$ and $\Delta < 0$, while nontopological gapped phases arise at $|\mu| > 2|\omega|$.

Mechanical systems of magnetically coupled spinners [43–46] have recently been used to simulate a number of electronic tight-binding Hamiltonians. The spinner ladder system pictured in Fig. 1(a) shows the metamaterial analog of the SSH ladder in Fig. 1(b). Here the electron hopping translates to the interspinner magnetic interaction controlled by the distance between magnets, and the electronic eigenstate energy maps to the frequency squared (f^2) for the spinner normal modes. With magnets attached to selected spinner arms, nearest neighbors connected by the red, blue, and green lines in Fig. 1(b) have attractive interactions, parametrized by normalized positive constants β_r, β_b, and β_g, respectively. As marked by solid circles and open triangles in Fig. 1(b), the system is bipartite, and the rotations of the spinners are represented by θ_n and φ_n with $n = 1, \ldots, N$ within each sublattice for the system of length N. One of the spinners is driven externally, and attached accelerometers monitor oscillations. Details of the setup are provided in Appendix A and Refs. [43–45]. The normalized Lagrangian for the spinner system is

$$L = T - U_1 - U_2, \tag{2}$$

where

$$T = \frac{1}{8\pi^2} \sum_{n=1}^{N} \dot{\theta}_n^2 + \dot{\varphi}_n^2 \tag{3}$$

is the normalized kinetic energy, and

$$U_1 = \frac{\alpha}{2} \sum_{n=1}^{N} \theta_n^2 + \varphi_n^2 \tag{4}$$

with a positive coefficient α and

$$U_2 = \sum_n \beta_b \theta_n \varphi_{n+1} + \beta_r \theta_{n+1} \varphi_n + \beta_g \theta_n \varphi_n \tag{5}$$

TABLE I. Mapping between the parameters of the SSH spinner ladder system [Eq. (5)] and the electronic Kitaev chain [Eq. (1)]. For the spinner system, the θ_n and φ_n represent the rotation angles of the spinners, the β_b and β_r the *intrachain* interactions, and the β_g the *interchain* interaction, as shown in Figs. 1(b) and 1(d). For the Kitaev chain, a_n and b_n are the Majorana operators, ω the nearest-neighbor electron hopping amplitude, Δ the p-wave superconducting order parameter, and μ the chemical potential [37].

SSH spinner ladder system	θ_n	φ_n	β_b	β_r	β_g
Electronic Kitaev chain	a_n	b_n	$\omega - \Delta$	$\omega + \Delta$	μ

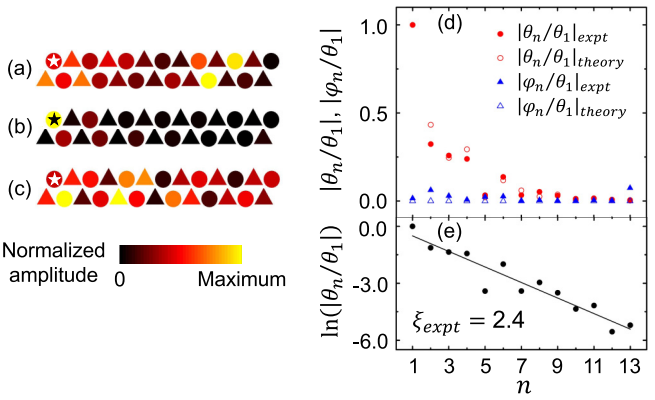

FIG. 2. Localization of the MLBS for a system with $N = 13$ and $\beta_g = 100$ Hz^2, a case in Fig. 1(c). (a)–(c) Rotational oscillation amplitudes of spinners measured for (a) an upper bulk mode, (b) a midgap MLBS, and (c) a lower bulk mode. (See Supplemental Material [47] for videos.) The color represents the rotational oscillation amplitude of each spinner. The stars mark the actuated spinners. (d) Normalized rotational oscillation amplitudes, $|\theta_n/\theta_1|$ (red circles) and $|\varphi_n/\theta_1|$ (blue triangles), versus n. The solid and open symbols represent the experimental and theoretical results. (e) Symbols: semilogarithmic plot of $\ln|\theta_n/\theta_1|$ versus n for the experiments. Line: linear fit giving a localization length $\xi_{\text{expt}} = 2.4$, consistent with the theory.

represent the normalized potential energy. While the term U_1 shifts the spectrum by a constant, the term U_2 has the form identical to H_{K} in Eq. (1), depicted by the mapping shown in Table I. This mapping allows us to explore the analogy between the metamaterials and electronic systems through direct excitations of spinners, as shown in videos in the Supplemental Material [47].

In long ladders, we observe a clear phase transition between nontopological and topological phases characterized by midgap MLBSs as a function of the interaction between SSH chains, which is analogous to the chemical potential in the Kitaev chain. Figure 1(c) shows f^2 for normal modes versus the interchain coupling β_g for the $N = 13$ spinner systems [see Figs. 1(a) and 1(b)] with intrachain couplings $\beta_r = 230$ Hz^2 and $\beta_b = 100$ Hz^2. Bulk modes, shown as black dots, are identified from the resonant oscillations of spinners near the center of the system. In contrast, the red dot in the spectrum corresponds to the MLBS at one of the system's ends, and is prominently identified from measurement of the θ_1 spinner. We expect another MLBS mode at the other end at the same frequency. (See Appendix B for typical spectra.) Starting from large interchain coupling β_g, the gap in the bulk spectra rapidly narrows as β_g decreases, and closes when $\beta_g \approx 310$ Hz^2, consistent with the theoretical phase boundary $\beta_{g,c} = \beta_r + \beta_b = 330$ Hz^2 (see the top axis). As β_g decreases further, the gap reopens but with a distinct midgap mode, which marks the topological phase transition. Bulk bands fall within the theoretically predicted range for the infinitely long ladder system [37] shown in gray. We conclude that the $N = 13$ spinner system realizes the long ladder limit, thus expanding on the results in Ref. [39], where finite size effects presented more of a limitation. (See Appendix B for gap versus β_g and theoretical ranges for bulk bands.)

Realizing the short topological systems, we find that MLBSs from the two ends overlap, and therefore the degenerate end modes of the long limit hybridize and split in frequency, in close analogy to hybridization of MZM wave functions. To first order, the split modes correspond to symmetric and antisymmetric combinations of the MLBS up to a tunable relative phase. For the infinitely long topological system, theory predicts that MLBSs reside on the θ_n sublattice at the left edge and on the φ_n sublattice at the right edge if $\beta_r > \beta_b$ (as in all cases in this Letter). For the short topological system with $N = 5$, schematically shown in Fig. 1(d), the hybridization and splitting is evident in Fig. 1(e), where the normalized amplitudes measured at the θ_1 (φ_5) spinner are plotted with respect to f^2 within the gap in red (blue) dots. To reveal the impact of the significant overlap of the two peaks, we measure the angles θ_1 and φ_5 versus time at three frequencies indicated by the dashed lines in Fig. 1(e), that is, the lower and upper MLBS frequencies, and a frequency in between, as shown in Figs. 1(g), 1(i), and 1(h), respectively. The phase differences between φ_5 and θ_1, $\eta(\varphi_5) - \eta(\theta_1)$, are 0.77π and 0.07π for the lower and upper MLBSs. In being close to π or 0, they mimic the theoretical results for an ideal system without damping, that is, odd or even symmetry. Similarly, for a series of frequencies in the gap, the relative phase $\eta(\varphi_5) - \eta(\theta_1)$ is plotted as dots in Fig. 1(f). It shows a continuous change of the phase difference, in agreement with theoretical results for a damped system shown in a green line. Here, we emphasize that the tunability of the relative phase in our system may have future applications in mechanical memories [48].

Importantly, MLBSs are not only bipartite and decaying, but also characterized by spatial oscillations. For instance, for the topological $N = 13$ system with $\beta_g = 100$ Hz^2 in Fig. 1(c), rotational oscillation amplitudes of the spinners for the MLBS are displayed in colors in Fig. 2(b). Here, it is revealed that the MLBS resides mostly on the θ_n sites (circles) near the left edge, unlike typical bulk modes shown in Figs. 2(a) and 2(c). (See Supplemental Material for videos [47].) The detailed structure of the MLBS is seen in Fig. 2(d), where the normalized amplitude for the θ_n ($|\theta_n/\theta_1|$, red solid circles) is large near the left edge, while amplitude for the φ_n ($|\varphi_n/\theta_1|$, blue solid triangles) is negligible. These results qualitatively agree with Ref. [39], but with an important difference: in our system the decaying amplitude *oscillates*. Moreover, this oscillation rather successfully matches theoretical predictions [42] and is the first to realize them.

For MZMs in the Kitaev chain, theory [42] predicts such oscillatory wave functions within a circle in the phase diagram set by $\mu^2 + (2\Delta)^2 < (2\omega)^2$. Translated to the spinner system, the spatial profile of the MLBS localized at the left edge is given by

$$\theta_n = A \exp\left(-\frac{n}{\xi_{\text{theory}}}\right) \cos\left(B + \frac{2\pi n}{\lambda}\right) \tag{6}$$

if $\beta_g < \beta_{g,o}$, where $\xi_{\text{theory}} = 2[\ln(\beta_r/\beta_b)]^{-1}$ is the localization length, λ, A, and B are constants, and $\beta_{g,o} = 2\sqrt{\beta_b \beta_r}$. (See Appendix C for details.) For the system in Fig. 2, $\beta_g = 100\ \text{Hz}^2$ is indeed less than $\beta_{g,o} = 300\ \text{Hz}^2$ [see the top axis in Fig. 1(c)], and the theoretical results for the $|\theta_n/\theta_1|$ and $|\varphi_n/\theta_1|$ plotted in open symbols in Fig. 2(d) agree well with the experiments. Further, a linear fit of $\ln|\theta_n/\theta_1|$ versus n for the experiments shown in Fig. 2(e) results in $\xi_{\text{expt}} = 2.4$, identical to the theoretical value ξ_{theory}. Strong agreement with the theory confirms that the spatial oscillation seen here is not due to disorder, but reflects the intrinsic nature of the MLBS spatial profiles, analogous to the oscillatory MZM wave functions.

The oscillatory behavior of the MLBSs significantly affects spectral features of the system. Most importantly, when their hybridization changes its sign, there is a switch between whether the symmetric or the antisymmetric combination corresponds to the lower frequency. In the MZM analog, this behavior results in so-called parity switching [40–42,49]. Here, consequences of the switch are rather profound: the two end MZMs form a Dirac fermionic state that can be occupied or unoccupied, essentially a topological qubit, thus giving the system odd or even parity. In other words, the sign of the hybridization determines ground state parity. To demonstrate the analog of this switching in the topological spinner systems, we vary the length of the system, $N = 3, 4, \ldots, 8$, while keeping the interactions identical to Figs. 1(d)–1(i). Normalized amplitudes of the φ_N spinner (resulting from actuating the θ_1 spinner) versus f^2 within the bulk gap are shown as *solid* symbols in Fig. 3(a). The split of the MLBSs, indicated by yellow areas in Fig. 3(a) and solid circles in Fig. 3(b), clearly oscillates as N increases, in agreement with theoretical results, shown as open circles in Fig. 3(b). Behavior of the spinner system analogous to parity switching is most evident in the phase difference between the φ_N and θ_1 spinner, $\eta(\varphi_N) - \eta(\theta_1)$, versus f^2 shown as *open* symbols in Fig. 3(a). The phase difference changes approximately from π to 0 as the frequency increases for $N = 5$ and 8, but from 0 to $-\pi$ for $N = 3$, 4, 6, and 7. The observed switch in the phase difference for the upper MLBS is displayed in Fig. 3(b) using the background color for each N, that is, blue for $\eta(\varphi_N) - \eta(\theta_1) \approx 0$ (even symmetry) and red for $\pm\pi$ (odd). It agrees with the theory except for the $N = 4$ case (purple, odd from the experiments, but even from the theory) [42,50]. The phase switching seen here may prove to be a consequential feature when it comes to designing MZM qubits, because it strengthens the proposal that the chemical potential be tuned to achieve exactly degenerate MZMs in finite Kitaev chains [40–42].

In conclusion, demonstrating the potentiality of research that connects electronic and metamaterial systems, we analyzed surprisingly close analogs of MZMs in Kitaev chains with MLBSs in spinner ladders. While the degrees of freedom differ, our in-depth realization provides a well-controlled prototype for benchmarking any MZMs that may be discovered in the future [51]. Further, our studies signal promise for next-generation metamaterial applications, such as topological braiding of midgap states in the case of stacked SSH ladders [36]. From the metamaterials perspective, states like MLBSs offer wide possibilities, such as mechanical memory and device applications.

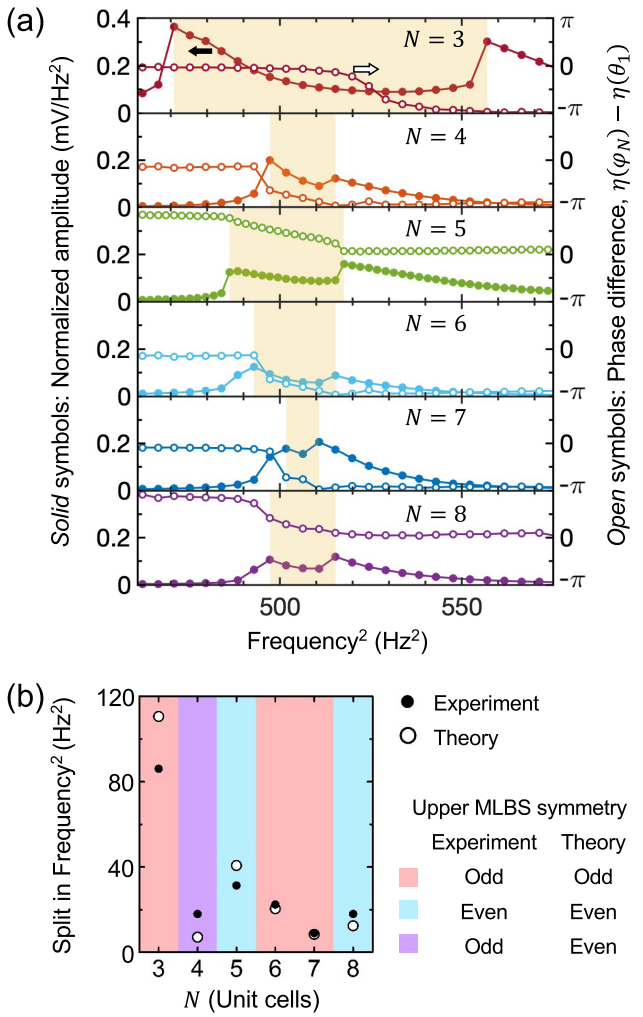

FIG. 3. Split oscillation and phase difference switching of the hybridized MLBSs as varying the length of the systems. (a) *Solid* symbols: Spectra of the topological systems for $N = 3, 4, \ldots, 8$, obtained by actuating θ_1 and measuring at φ_N spinners for the frequencies within the bulk gap. The interactions are kept identical to those in Figs. 1(d)–1(i). The widths of the yellow areas represent the splits of the hybridized MLBSs. *Open* symbols: The corresponding phase differences, $\eta(\varphi_N) - \eta(\theta_1)$. (b) Symbols: Split between the hybridized MLBSs versus the length of the system, N, for the experiments (solid symbols) and the theory (open symbols). Background colors: Observed phase difference of the upper MLBS is shown in blue for close to 0 (even symmetry) and red for $\pm\pi$ (odd), agreeing with the theory. A disagreement between theory and experiments occurs for the $N = 4$ case, shown in purple, likely due to disorder in the experimental setup [50].

K.Q. and C.P. acknowledge support from the W. M. Keck Foundation. C.P. acknowledges support from National Science Foundation (NSF Award 2131759). K.Q., K.H.A., and C.P. acknowledge support from NJIT Faculty Seed Grant. S.V. acknowledges support from the National Science Foundation and the Quantum Leap Challenge Institute for Hybrid Quantum Architectures and Networks (NSF Award 2016136).

APPENDIX A: DETAILS OF EXPERIMENTAL SETUP

The system is made up of two parallel SSH chains with alternating *intrachain* couplings, shifted with respect to each other and coupled by a constant *interchain* interaction. Each spinner has six arms with magnets attached to the arms in the 0°, 180°, and 240° (0°, 60°, and 180°) directions for the top (bottom) chain, as highlighted in Fig. 1(a) in the main text. The red, blue, and green lines in Fig. 1(b) indicate different nearest-neighbor interactions, represented by the normalized positive parameters β_r, β_b, and β_g between the magnets separated by the distances $d_r = 5.0$ mm, $d_b = 8.0$ mm, and d_g, respectively. The root-mean-square voltages from attached accelerometers divided by frequency squared (f^2) are used as the quantities proportional to the oscillation amplitudes.

APPENDIX B: TYPICAL SPECTRA, GAP VERSUS INTERCHAIN COUPLING β_g, AND THEORETICAL RANGES FOR BULK BANDS

Typical spectra of the normalized amplitude versus f^2 for the long $N = 13$ ladder systems are shown in Figs. 4(a), 4(b), and 4(c) for the topological insulator, metallic, and nontopological insulator cases, respectively (see the left panels in Fig. 1 in the main text).

According to the theory [37] for the infinitely long SSH ladder system, the outer boundaries of the bulk bands are at

$$f^2 = \alpha \pm (\beta_r + \beta_b + \beta_g), \tag{B1}$$

while the inner boundaries are at

$$f^2 = \alpha \pm |\beta_r + \beta_b - \beta_g|, \quad \text{if } \beta_g > \beta_{g,G}, \tag{B2}$$

$$f^2 = \alpha \pm |\beta_r - \beta_b|\sqrt{1 - \beta_g^2/4\beta_b\beta_r}, \quad \text{if } \beta_g < \beta_{g,G}, \tag{B3}$$

where $\beta_{g,G} = 4\beta_b\beta_r/(\beta_b + \beta_r)$. With the parameters for the systems studied, we obtain $\beta_{g,G} = 280$ Hz^2 indicated on the top axis in Fig. 4(d), and the ranges for the upper and lower bulk bands shown as the gray areas in Fig. 1(c) in the main text. The theoretical gap size G_{theory} is found to be

$$G_{\text{theory}} = 2|\beta_r + \beta_b - \beta_g|, \quad \text{if } \beta_g > \beta_{g,G}, \tag{B4}$$

$$G_{\text{theory}} = 2|\beta_r - \beta_b|\sqrt{1 - \beta_g^2/4\beta_b\beta_r}, \quad \text{if } \beta_g < \beta_{g,G}. \tag{B5}$$

The gap sizes versus the interchain coupling β_g for the experiments and theory are displayed as dots and lines, respectively, in Fig. 4(d), showing a good agreement.

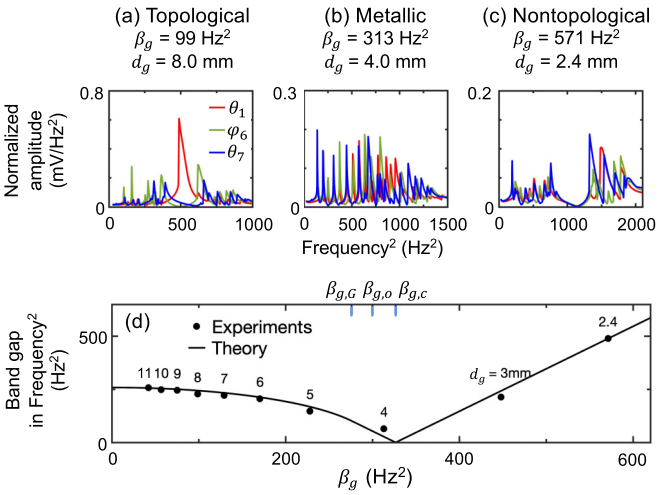

FIG. 4. (a)–(c) Spectra measured for the long $N = 13$ ladder systems with the interchain coupling $\beta_g = 99$, 313, and 571 Hz^2 to show the examples of the spectra for the topological insulator, metallic, and nontopological insulator phases, respectively. The red, green, and blue lines represent the spectra obtained by actuating the θ_1, φ_6, and θ_7 spinners, respectively, and measuring at the same spinners. Each peak corresponds to a mode, shown as a dot in Fig. 1(c) in the main text. The peak for the midgap MLBS is prominent in the topological phase, as seen from the red line in (a), and is represented as a red dot in Fig. 1(c). (d) Band gap versus β_g, showing topological phase transition as β_g decreases from around 600 Hz^2. The dots and lines represent the experimental and theoretical results, respectively. The numbers above the dots represent the intermagnet distances, d_g, between the two SSH chains. The three tick marks on the top axis represent the three critical values of β_g, that is, $\beta_{g,c}$ for the gap closing, $\beta_{g,o}$ for the oscillatory MLBS spatial profile, and $\beta_{g,G}$ for the gap function, as discussed in the main text and Appendices B and C.

APPENDIX C: DETAILS OF MLBS SPATIAL PROFILE FROM THEORY

The theory [42] predicts that the MLBS localized at the left edge for the infinitely long ladder system satisfies $\varphi_n = 0$, $\theta_{n+1} = -\theta_n\beta_g/\beta_r - \theta_{n-1}\beta_b/\beta_r$, and $\theta_2 = -\theta_1\beta_g/\beta_r$. Depending on the sign of $\beta_g - \beta_{g,o}$, where $\beta_{g,o} = 2\sqrt{\beta_b\beta_r} < \beta_{g,c}$, the solution for θ_n has different forms:

$$\theta_n = Ae^{-n/\xi}\cos(B + 2\pi n/\lambda), \quad \text{if } \beta_g < \beta_{g,o}, \tag{C1}$$

$$\theta_n = (A + Bn)e^{-n/\xi}, \quad \text{if } \beta_g = \beta_{g,o}, \tag{C2}$$

$$\theta_n = Ae^{-n/\xi_+} + Be^{-n/\xi_-}, \quad \text{if } \beta_{g,o} < \beta_g < \beta_{g,c}, \tag{C3}$$

where $\xi = 2[\ln(\beta_r/\beta_b)]^{-1}$ and $\xi_\pm = 1/\ln\{2\beta_r/[\beta_g \pm (\beta_g{}^2 - 4\beta_b\beta_r)^{1/2}]\}$ are the localization lengths, $\lambda = 2\pi/\arccos(-\beta_g/2\sqrt{\beta_r\beta_b})$ is the wavelength, and A and B are constants.

[1] E. Prodan and C. Prodan, Topological Phonon Modes and Their Role in Dynamic Instability of Microtubules, Phys. Rev. Lett. **103**, 248101 (2009).

[2] S. D. Huber, Topological mechanics, Nat. Phys. **12**, 621 (2016).

[3] C. L. Kane and T. C. Lubensky, Topological boundary modes in isostatic lattices, Nat. Phys. **10**, 39 (2014).

[4] B. G.-G. Chen, B. Liu, A. A. Evans, J. Paulose, I. Cohen, V. Vitelli, and C. D. Santangelo, Topological Mechanics of Origami and Kirigami, Phys. Rev. Lett. **116**, 135501 (2016).

[5] P. Gao, D. Torrent, F. Cervera, P. San-Jose, J. Sánchez-Dehesa, and J. Christensen, Majorana-like Zero Modes in Kekulé Distorted Sonic Lattices, Phys. Rev. Lett. **123**, 196601 (2019).

[6] B. G.-G. Chen, N. Upadhyaya, and V. Vitelli, Nonlinear conduction via solitons in a topological mechanical insulator, Proc. Natl. Acad. Sci. USA **111**, 13004 (2014).

[7] L. M. Nash, D. Kleckner, A. Read, V. Vitelli, A. M. Turner, and W. T. M. Irvine, Topological mechanics of gyroscopic metamaterials, Proc. Natl. Acad. Sci. USA **112**, 14495 (2015).

[8] P. Wang, L. Lu, and K. Bertoldi, Topological Phononic Crystals with One-Way Elastic Edge Waves, Phys. Rev. Lett. **115**, 104302 (2015).

[9] E. Majorana, Teoria simmetrica dell'elettrone e del positrone, Nuovo Cimento **14**, 171 (1937).

[10] A. Y. Kitaev, Fault-tolerant quantum computation by anyons, Ann. Phys. **303**, 2 (2003).

[11] C. Nayak, S. H. Simon, A. Stern, M. Freedman, and S. D. Sarma, Non-Abelian anyons and topological quantum computation, Rev. Mod. Phys. **80**, 1083 (2008)

[12] F. Wilczek, Majorana returns, Nat. Phys. **5**, 614 (2009).

[13] R. M. Lutchyn, J. D. Sau, and S. D. Sarma, Majorana Fermions and a Topological Phase Transition in Semiconductor-Superconductor Heterostructures, Phys. Rev. Lett. **105**, 077001 (2010).

[14] Y. Oreg, G. Refael, and F. von Oppen, Helical Liquids and Majorana Bound States in Quantum Wires, Phys. Rev. Lett. **105**, 177002 (2010).

[15] J. Alicea, New directions in the pursuit of Majorana fermions in solid state systems, Rep. Prog. Phys. **75**, 076501 (2012).

[16] P. Hosur, P. Ghaemi, R. S. K. Mong, and A. Vishwanath, Majorana Modes at the Ends of Superconductor Vortices in Doped Topological Insulators, Phys. Rev. Lett. **107**, 097001 (2011).

[17] M. Leijnse and K. Flensberg, Introduction to topological superconductivity and Majorana fermions, Semicond. Sci. Technol. **27**, 124003 (2012).

[18] J. C. Teo and T. L. Hughes, Existence of Majorana-Fermion Bound States on Disclinations and the Classification of Topological Crystalline Superconductors in Two Dimensions, Phys. Rev. Lett. **111**, 047006 (2013).

[19] S. Nadj-Perge, I. K. Drozdov, J. Li, H. Chen, S. Jeon, J. Seo, A. H. MacDonald, B. A. Bernevig, and A. Yazdani, Observation of Majorana fermions in ferromagnetic atomic chains on a superconductor, Science **346**, 602 (2014).

[20] M. Sato and S. Fujimoto, Majorana fermions and topology in superconductors, J. Phys. Soc. Jpn. **85**, 072001 (2016).

[21] A. Y. Kitaev, Unpaired Majorana fermions in quantum wires, Phys. Usp. **44**, 131 (2001).

[22] *Logic and Algebraic Structures in Quantum Computing*, edited by J. Chubb, A. Eskandarian, and V. Harizanov (Cambridge University Press, Cambridge, 2016).

[23] B. Lian, X. Q. Sun, A. Vaezi, X. L. Qi, and S. C. Zhang, Topological quantum computation based on chiral Majorana fermions, Proc. Natl. Acad. Sci. USA **115**, 10938 (2018).

[24] R. Aguado and L. Kouwenhoven, Majorana qubits for topological quantum computing, Phys. Today **73**(6), 44 (2020).

[25] C. Tutschku, R. W. Reinthaler, C. Lei, A. H. MacDonald, and E. M. Hankiewicz, Majorana-based quantum computing in nanowire devices, Phys. Rev. B **102**, 125407 (2020).

[26] T. L. Hughes, Majorana fermions inch closer to reality, Physics **4**, 67 (2011).

[27] V. Mourik, K. Zuo, S. M. Frolov, S. R. Plissard, E. P. A. M. Bakkers, and L. P. Kouwenhoven, Signatures of Majorana fermions in hybrid superconductor-semiconductor nanowire devices, Science **336**, 1003 (2012).

[28] L. P. Rokhinson, X. Liu, and J. K. Furdyna, The fractional a.c. Josephson effect in a semiconductor-superconductor nanowire as a signature of Majorana particles, Nat. Phys. **8**, 795 (2012).

[29] A. Das, Y. Ronen, Y. Most, Y. Oreg, M. Heiblum, and H. Shtrikman, Zero-bias peaks and splitting in an Al-InAs nanowire topological superconductor as a signature of Majorana fermions, Nat. Phys. **8**, 887 (2012).

[30] S. M. Albrecht, A. P. Higginbotham, M. Madsen, F. Kuemmeth, T. S. Jespersen, J. Nygård, P. Krogstrup, and C. M. Marcus, Exponential protection of zero modes in Majorana islands, Nature (London) **531**, 206 (2016).

[31] M. T. Deng, S. Vaitiekenas, E. B. Hansen, J. Danon, M. Leijnse, K. Flensberg, J. Nygård, P. Krogstrup, and C. M. Marcus, Majorana bound state in a coupled quantum-dot hybrid-nanowire system, Science **354**, 1557 (2016).

[32] R. M. Lutchyn, E. P. A. M. Bakkers, L. P. Kouwenhoven, P. Krogstrup, C. M. Marcus, and Y. Oreg, Majorana zero modes in superconductor-semiconductor heterostructures, Nat. Rev. Mater. **3**, 52 (2018).

[33] Z. Wang, J. O. Rodriguez, L. Jiao, S. Howard, M. Graham, G. D. Gu, T. L. Hughes, D. K. Morr, and V. Madhavan, Evidence for dispersing 1D Majorana channels in an iron-based superconductor, Science **367**, 104 (2020).

[34] S. Vishveshwara and D. M. Weld, Z_2 phases and Majorana spectroscopy in paired Bose-Hubbard chains, Phys. Rev. A **103**, L051301 (2021).

[35] A. McDonald, T. Pereg-Barnea, and A. A. Clerk, Phase-Dependent Chiral Transport and Effective Non-Hermitian Dynamics in a Bosonic Kitaev-Majorana Chain, Phys. Rev. X **8**, 041031 (2018).

[36] Y. Barlas and E. Prodan, Topological Braiding of Non-Abelian Midgap Defects in Classical Metamaterials, Phys. Rev. Lett. **124**, 146801 (2020).

[37] K. Padavić, S. S. Hegde, W. DeGottardi, and S. Vishveshwara, Topological phases, edge modes, and the Hofstadter butterfly in coupled Su-Schrieffer-Heeger systems, Phys. Rev. B **98**, 024205 (2018).

[38] W. P. Su, J. R. Schrieffer, and A. J. Heeger, Solitons in Polyacetylene, Phys. Rev. Lett. **42**, 1698 (1979).

[39] Z. Guo, J. Jiang, H. Jiang, J. Ren, and H. Chen, Observation of topological bound states in a double Su-Schrieffer-Heeger chain composed of split ring resonators, Phys. Rev. Res. **3**, 013122 (2021).

[40] H.-C. Kao, Chiral zero modes in superconducting nanowires with Dresselhaus spin-orbit coupling, Phys. Rev. B **90**, 245435 (2014).

[41] S. Hegde, V. Shivamoggi, S. Vishveshwara, and D. Sen, Quench dynamics and parity blocking in Majorana wires, New J. Phys. **17**, 053036 (2015).

[42] S. S. Hegde and S. Vishveshwara, Majorana wave-function oscillations, fermion parity switches, and disorder in Kitaev chains, Phys. Rev. B **94**, 115166 (2016).

[43] D. J. Apigo, K. Qian, C. Prodan, and E. Prodan, Topological edge modes by smart patterning, Phys. Rev. Mater. **2**, 124203 (2018).

[44] K. Qian, D. J. Apigo, C. Prodan, Y. Barlas, and E. Prodan, Topology of the valley-Chern effect, Phys. Rev. B **98**, 155138 (2018).

[45] K. Qian, L. Zhu, K. H. Ahn, and C. Prodan, Observation of Flat Frequency Bands at Open Edges and Antiphase Boundary Seams in Topological Mechanical Metamaterials, Phys. Rev. Lett. **125**, 225501 (2020).

[46] L. Zhu, E. Prodan, and K. H. Ahn, Flat energy bands within antiphase and twin boundaries and at open edges in topological materials, Phys. Rev. B **99**, 041117(R) (2019).

[47] See Supplemental Material at http://link.aps.org/supplemental/10.1103/PhysRevResearch.5.L012012 for the slow motion videos of bulk modes and MLBSs for Figs. 1(g), 1(i), 2(a), 2(b), and 2(c).

[48] M. A. Hasan, K. Runge, and P. A. Deymier, Experimental classical entanglement in a 16 acoustic qubit-analogue, Sci. Rep. **11**, 24248 (2021).

[49] J. Ávila, E. Prada, P. San-Jose, and R. Aguado, Majorana oscillations and parity crossings in semiconductor nanowire-based transmon qubits, Phys. Rev. Res. **2**, 033493 (2020).

[50] The difference between theory and experiments for the $N = 4$ system is likely originated from disorders present in the experimental setup. For example, the two theoretically predicted MLBS peaks are close enough that they could be switched in the experiments due to disorders. A possible source of the disorders includes the moments of inertia of the attached accelerometers.

[51] J. Sau, S. Simon, S. Vishveshwara, and J. R. Williams, From anyons to Majoranas, Nat. Rev. Phys. **2**, 667 (2020).